Statistics of branched fracture surfaces

E. Bouchaud
Office National d'Etudes et de Recherches Aérospatiales (OM), 29, Avenue de la Division Leclerc, Boîte Postale 72, F-92322 Châtillon Cedex, France
and University of Cambridge, Department of Materials Science and Metallurgy, Pembroke Street, Cambridge CB2 3QZ, England

G. Lapasset, J. Planès, and S. Naveos
Office National d'Etudes et de Recherches Aérospatiales (OM), 29, Avenue de la Division Leclerc, Boîte Postale 72, F-92322 Châtillon Cedex, France
(Received 1 March 1993; revised manuscript received 4 May 1993)

A statistical analysis of fracture surfaces of the polycrystalline intermetallic compound Ni_3Al is reported. Although these surfaces contain secondary branches, a roughness exponent ζ can be defined, and is found close to 0.8. The number of branches is shown to have nontrivial fluctuations, which exhibit a power-law increase with an exponent strongly dependent upon the dynamics of crack branching during crack propagation. Moreover, the probability distributions of both heights and averaged heights are shown to slowly decrease, i.e., like power laws, for high enough altitudes. Dynamical effects could be responsible for these "anomalous" statistics.

INTRODUCTION

Since the pioneering work of Mandelbrot, Passoja, and Paullay,[1] numerous experimental measurements of the fractal dimension of fracture surfaces were performed on various materials using various experimental methods.[2–9] Many of these experiments aimed to establish a correlation between this dimension and macroscopic fracture parameters, such as the fracture toughness or the impact energy measured during Charpy tests. In Ref. 1, the authors concluded that for their series of steels, the higher the fractal dimension, i.e., the rougher the surface, the lower the impact energy. The opposite correlation was observed on some ceramics by other authors.[2] However, in all the quoted references, variations of the fractal dimension are rather small (range 2.1–2.3), and in most cases, no experimental error bars are estimated.

Experiments performed on four samples of the 7475 aluminum alloy[6,7] subjected to four different heat treatments, which produced four different fracture modes and fracture toughnesses, resulted in identical roughness exponents ζ [in the case of self-affine surfaces, ζ is related to the "box" fractal dimension d_f (Ref. 10) through the relation $d_f=3-\zeta$], within experimental accuracy. It was conjectured[6,7,11] that the value 0.8 of ζ could be universal, i.e., independent of the micromechanisms of fracture and of the material. In a recent publication of Måløy *et al.*,[8] values of ζ close to 0.8 were also reported for a series of various brittle materials.

Experiments are performed on the intermetallic compound Ni_3Al, which is well known to be prone to brittle intergranular fracture.[12] The surfaces of the two studied samples contain many secondary branches and overhangs and do not look like simple "mountain landscapes." This seems to be very common in the field of intermetallic-based alloys.[13] Nevertheless, a roughness exponent can be defined through the return-probability power-law behavior (see below). In the three series of experiments, this exponent is found close to 0.8. On the other hand, it is a well-known result,[14–16] although not fully understood,[17–21] that fast-running cracks branch when a critical velocity is overpassed. One can reasonably expect that this is the case for most intermetallics in a fracture toughness experiment. The fluctuations of the number of secondary cracks are shown to exhibit a power-law behavior with an exponent close to 0.13. The value of this exponent should be strongly related to the dynamics of crack branching.

The conditional probability distribution $P(r,z)$ of finding the point (r,z) on the surface, averaged over all possible origins belonging to the surface is shown to exhibit a scaling behavior:

$$P(r,z)=\frac{1}{r^{\zeta}}f\left[\frac{z}{r^{\zeta}}\right] , \tag{1}$$

with $f(u)$ decreasing very slowly $(\sim 1/u)$ for high enough values of u. The broad character of this distribution should be due mainly to the presence of secondary cracks. The whole structure under study can be viewed as a "fluffy" fractal, with branches growing from a structure with roughness index 0.8.

The conditional probability $P_m(r,\bar{z}(r))$ is also computed. $P_m(r,\bar{z}(r))$ describes the distribution of the height $\bar{z}(r)$ which is the average value of the heights at point r:

$$\bar{z}(r)=\frac{1}{n(r)}\sum_{i=1}^{n(r)} z_i(r) , \tag{2}$$

where $z_i(r)$ are the heights of the points located on the fracture surface with the same abscissa r, and $n(r)$ is the number of such points. In the following, $n(r)$ will be called "the number of branches at point r," although the secondary structures may either be secondary cracks or

0163-1829/93/48(5)/2917(12)/$06.00

overhangs. $P_m(r,\bar{z}(r))$ also exhibits a scaling behavior with slowly decreasing tail:

$$P_m(r,\bar{z}(r))=\frac{1}{r^{\zeta}}g\left[\frac{\bar{z}}{r^{\zeta}}\right], \tag{3}$$

with

$$g(u)\sim\frac{1}{u^{1.67}} . \tag{4}$$

This is in good agreement with the results obtained on the various moments of P_m:

$$M_q(r)=\langle(|\bar{z}(x+r)-\bar{z}(x)|)^q\rangle_x \tag{5}$$

where q is an integer and the average $\langle\ \rangle_x$ is performed over all possible values of the origin x. These moments do exhibit power-law behaviors, but with exponents different from $q\zeta$ for all the values of q under consideration ($q=2,3,4,5,6$). This contrasts strongly with recent results due to Hansen *et al.*;[22] in Ref. 22, the ratios

$$\frac{[M_q(r)]^{1/q}}{[M'_q(r)]^{1/q'}} \tag{6}$$

were reported to be independent of r for a series of six different brittle materials. Furthermore, these ratios were found to fit a Gaussian distribution. However, no fracture surface was reported to be branched in that case. The "anomalous" statistics which characterizes our surfaces could well be the signature of the dynamical instability which produces secondary cracks. Dynamical effects could also be at the origin of the discrepancy between the measured values of ζ, and the roughness index expected for a "minimum" surface.[23] Such a surface would *globally* minimize the fracture energy, by choosing at each elementary step the path leading to the minimum sum of all the elementary energies. It is not clear, however, how such an optimal configuration could be reached dynamically. This could explain that most available experiments[1–9] exclude the value 0.5, which should be close to the roughness index ζ (Refs. 24–26) of the minimum surface. One must note, however, that very recent measurements[27] on low cycle fatigue fracture surfaces suggest a value of 0.6. Tunneling scanning electron microscopy experiments, which deal with much smaller scales than ours (0.1–20 nm) also lead to exponents close to 0.4.[28,29] This discrepancy does not seem to hold for bidimensional systems. Simulations[11] on the random fuse model,[30,31] which does not take the dynamics into account, result in a universal value of ζ, i.e., independent of the disorder on a microscopic scale, which is close to the roughness exponent $\frac{2}{3}$ of the directed polymer in a random medium.[32,33] Experiments performed by Kertész, Horvath, and Weber[34] on tearing paper and by Poirier *et al.*[35] on cylinders are in perfect agreement with this value. It is worth mentioning also that a dynamical thermal fuse model was recently proposed by Vanneste and Sornette,[36] which leads to structures that, depending on a parameter of the model (the creep exponent), may have various fractal dimensions, and may contain many secondary branches.

I. MATERIAL AND EXPERIMENTAL PROCEDURE

A. Material and fracture

As far as Ni_3Al is concerned, the main objective was to obtain as large as possible intergranular fracture surfaces in order to improve their statistical analysis. So a small 14-mm thick plate of $Ni_{76}Al_{24}$ was prepared in an argon atmosphere by induction melting of pure constituents and casting onto a steel mold. The material was homogenized for 18 h at 1300 °C. Small rectangular chevron notch specimens ($2H=12$ mm, $B=17$ mm, $W=24$ mm) were machined and notched using electrodischarge machining.

A tensile stress was applied perpendicular to the chevron plane (mode I). However, during mechanical testing, as soon as the fracture started in the chevron plane, the crack abruptly deviated to a plane parallel to the applied stress, i.e., to the plate thickness direction, which is also the solidification direction. These "mode-II" cracks, with anisotropy axis perpendicular to the tensile axis are considered in the following. Optical examinations of the plate do not show any evidence of preexisting cracks or large porosity which could be due to the elaboration process (Fig. 1). Thus the secondary cracks observable on the fracture surfaces only appeared during tensile testing. This also means that deviation of the crack from the "mode-I" direction could be related either to an unsatisfactory geometry of the chevron notch specimens or to the anisotropy of crystallization and grain-boundary resistance. Indeed, although grains are rather equiaxed perpendicular to the plate thickness direction with a mean size about 0.5 mm, they exhibit heavy variations of size parallel to this direction (roughly from 200 μm to 5 mm) leading to a large aspect ratio for numerous grains (see Fig. 1).

Fracture surfaces were observed with a scanning electron micrograph Cambridge Stereoscan 100 with secondary electron contrast. They exhibit a pure intergranular

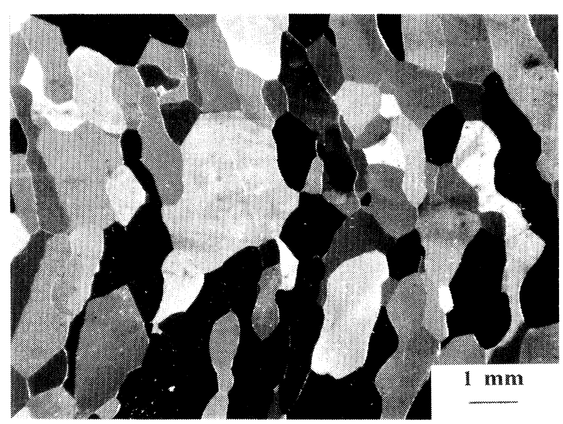

FIG. 1. Optical macrograph showing the etched surface (Fry Etch) of the Ni_3Al material prior to fracture. One can note that the metallurgical grains are not isotropic; they are in fact elongated in the direction of the main crack. Both lengths and widths of the grains in the polishing plane appear to be rather broadly distributed.

aspect. Figure 2 reveals clearly the anisotropy of the grains, and the broad distribution of their widths. Note that the ultimate crack propagated parallel to the length of the grains. Figure 2 also reveals deep cracks branched on the main crack, which formed during fracture, as already emphasized (Fig. 1).

B. Preparation of the specimens and image analysis

1. Preparation of the specimens

One of the samples was coated with opaque resin (sample 1), while the other one was electrochemically NiPd-plated (sample 2). Both were polished parallel to the anisotropy axis, and *perpendicular to the direction of propagation of the crack,* thus showing the separation "line" between the metal and the deposit. Let us emphasize that the various probability distributions are computed within that plane. In the following, the separation line between the intermetallic and the deposit will be referred to as "the profile." Only one cut was obtained from sample 1, while we made two consecutive cuts on sample 2. These three surfaces gave rise to three sets of experiments which will be referred to as 1 (sample 1), 2 (sample 2, first cut), and 3 (sample 2, second cut) hereafter (see Table I).

As the wetting of the resin on the metal is not perfect, and because of the large hardness difference between the two materials, sample 1 cannot be observed at a magnitude greater than $\times 75$. An optical microscope Olympus PMG3 is used for that purpose. Figure 3 shows an optical micrograph of sample 1. One can see both the secondary cracks and the cut of the overhangs linked to the fracture surface in planes which lie beside the polishing plane. A few of these overhangs are relatively far from the fracture surface (some grain widths). Surfaces 2 and 3 are observed at various magnifications with scanning electron microscopes—respectively, Zeiss DSM 960 and Cambridge Stereoscan 100—using a backscattered electron contrast.

2. Image analysis

The negatives of three micrographs (magnifications from $\times 32$ to $\times 75$) obtained from experiment 1 are recorded using a CCD camera Lhesa 506 N (with objective lens Micronikkor 55 mm) and digitized to 758×512 pixels images over 256 grey levels using the Synoptics Synergy Board mounted on an IBM PC 486-33. In experiments 2 and 3, the scanning microscopes are remotely monitored by a Kevex Delta system, which directly provides digitized pictures. In experiment 2, the size of the images is 703×512 pixels, while in experiment 3, their size is 186×512 pixels (see Table I). Five and seven micrographs (magnifications $\times 20$ to $\times 200$) were analyzed in experiments 2 and 3, respectively. Image analysis is performed by the Synoptics Semper 6 software facilities. The frontiers between the metal and the coating are extracted from the binarized images. In each case, the images are abandoned whenever edge detection is not straightforward. For the low magnifications used, however, this problem usually does not arise, since the contrast is rather high.

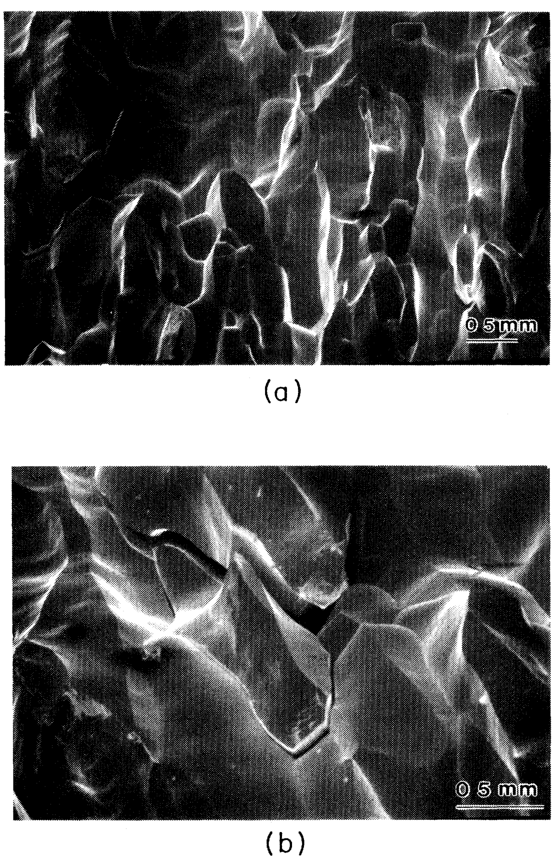

FIG. 2. Micrographs taken with a scanning electron microscope Cambridge Stereoscan 100. (a) and (b) both show the fracture surfaces, at two different magnifications. The fracture mode is clearly intergranular. (a) gives an idea of the anisotropy of the grains, as well as of the broad character of their widths distribution. (b) clearly shows the presence of deep secondary cracks.

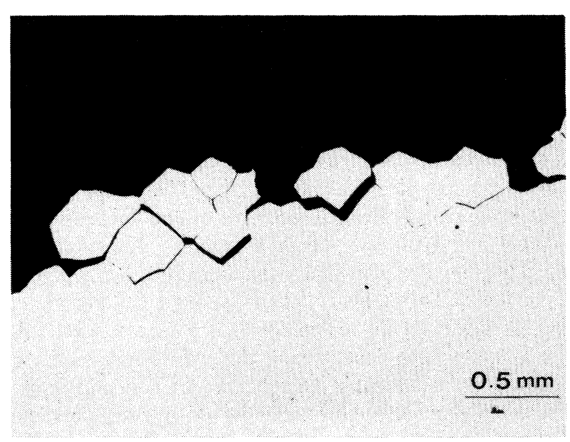

FIG. 3. Experiment 1. Optical micrograph Olympus PMG3. The fracture surface is coated with an opaque resin. The "vertical" cut reveals a branched profile. Note also the presence of overhangs, linked to the fracture surface in planes located beside the polishing plane.

TABLE I. Experiments 2 and 3. The magnifications are expressed in μm/pixel. The lengths ξ and z_0 are expressed in μm. Note that, although these lengths are not determined with a good precision, they fluctuate less in the case of experiment 2 than in the case of experiment 3. Exponent μ is only determined in the case of experiment 2, and is defined by $P(r,z)=(1/r^{\zeta})f(z/r^{\zeta})$ with $f(u)\sim 1/u^{1+\mu}$.

Ni$_3$Al: experiments 2 and 3						
Experiment	Image	Magnification	ζ	ξ	z_0	μ
2	2/1	5.066		203	350	0.08
	2/2	4.433		115	602	0.21
	2/3	5.910	0.82±0.03	195	302	0.08
	2/4	1.773		159	393	0.13
	2/5	2.533		251	590	−0.07
3	3/1	12.364		255	40	
	3/2	12.772		315	190	
	3/3	3.963		250	170	
	3/4	6.308	0.79±0.07	315	870	
	3/5	3.561		61	25	
	3/6	3.423		200	6	
	3/7	2.889		100	50	

C. Principle of the experimental method: a brief recall on self-affine surfaces

In this section, we briefly recall some properties relative to self-affine surfaces, for which most measurable quantities exhibit power-law behavior with all exponents related to the roughness index ζ. As it will be shown below, nearly all these quantities can be defined also for a multivalued set of heights, but have different behaviors.

The height $h(r)=[M_2(r)]^{1/2}$ of a profile of length r along an ordinary self-affine surface scales as

$$h(r)\sim r^{\zeta}\ , \tag{7}$$

where ζ is called the surface roughness exponent,[37] $\zeta<1$.

For such surfaces, it can be shown[37] that the return probability $P_0(r)$, which is the probability that the height comes back to its initial value $z=0$ after a distance r along the surface, scales as

$$P_0(r)=P(r,0)\equiv r^{-\zeta}f(0)\ , \tag{8}$$

where P and f are defined by Eq. (1). Note that for a usual self-affine the probabilities P and P_m are identical, since, for each point on the "horizontal" plane, there is only one intersection with the structure.

According to its definition, $P_0(r)$ is also the self-correlation $C(r)$ of the intersection of the surface and the horizontal $z=0$ plane. Thus polishing the surface perpendicularly to the z anisotropy axis and computing the self-correlation function $C(r)$ of the frontier between the metal and the coating, contained in this $z=$const plane, should, in principle, lead to the determination of ζ. $C(r)$ is obtained by averaging $C(\mathbf{r})$ over all directions in the horizontal plane, and $C(\mathbf{r})$ can be computed, for example, from the Fourier transform $P(\mathbf{q})$ of the occupation probability (the occupation probability being equal to 1 if the site is located on the cut, 0 otherwise), using the relation

$$|P(\mathbf{q})|^2=\mathcal{F}[C(\mathbf{r})]\ , \tag{9}$$

where $\mathcal{F}$ denotes a Fourier transform. This procedure was used in the case of the experiment reported in Refs. 6 and 7.

$P_0(r)$ may also be determined from the study of the profile extracted from a "vertical" (containing the z axis) cut of the surface. Such cuts were used by Måløy *et al.*[8] To compute P_0, one has to construct the histogram of horizontal distances r which correspond to the same height, and average it over all accessible values of the height. Note that this definition allows one to perform the computation of P_0 on a multivalued set of heights. In principle, one could determine in a similar manner the first return probability $P_1(r)$, i.e., the probability that the altitude goes back to its "initial" value z for the first time after a distance r in the horizontal plane. P_1 was shown to scale as[37]

$$P_1(r)\sim r^{-2+\zeta}\ , \tag{10}$$

but in our case the result is much too noisy to be useful. However, note that this quantity was computed successfully by Måløy *et al.*[8] These authors[8] also computed the one-dimensional power spectrum $\mathcal{P}(\omega)$ of the profile. Consistently with the values of ζ obtained from the analysis of P_1, they confirmed the power-law behavior

$$\mathcal{P}(\omega)\sim\omega^{-1-2\zeta}\ . \tag{11}$$

In our case, $\mathcal{P}(\omega)$ could not be computed because z is multivalued.

Finally, let us note that for ordinary self-affine surfaces, the moments M_q of the height defined in Eq. (5) all scale with exponents $q\zeta$:

$$M_q(r)\sim r^{\zeta(q)}\ , \tag{12}$$

with

$$\zeta(q)=q\zeta\ . \tag{13}$$

In the case of Ni$_3$Al, these moments are computed for the distribution P_m of the averaged heights. It will be shown in Sec. II that their scaling is quite different. Finally, the "number of branches" $n(r)$ at a given distance r in the horizontal plane is characterized through its fluctuations $N(r)$:

$$N(r)=\langle [n(r+x)-n(x)]^2\rangle_x^{1/2} \ . \tag{14}$$

II. EXPERIMENTAL RESULTS

Because of the anisotropy of the grains in the fracture plane, cuts perpendicular to the anisotropy axis cannot be performed. The study is thus restricted to profiles determined through cuts which contain the vertical axis z, and are perpendicular to the direction of propagation of the crack. The roughness index is measured through the determination of the return probability P_0.

A. Return probability P_0

For each experiment, the histogram $P_0(r)$ relative to one micrograph (number of values used equal to the length of the image), averaged on all values of z ($z=0$ being arbitrarily chosen) is reported on a log-log plot, which exhibits a linear portion extending from a distance comparable to the pixel size up to a distance ξ lying within the range of grain widths. Note that ξ being defined as the limit of the scaling domain, its value is only indicative (see Table I). For each micrograph, the extension of this zone is roughly two decades. For each experiment, curves relative to the various micrographs are reported on the same plot: $P_0(r)/P_0(\xi)$ versus r/ξ. "Roughness exponents" ζ can be determined in each case over two decades (see Fig. 4); values of ζ for experiments 2 and 3 are reported in Table I. Averaged results over the three sets of experiments read

$$\zeta=0.82\pm0.05 \ . \tag{15}$$

If the results of experiment 3, for which finite-size effects could be quite important (the images are 186 pixels long in experiment 3, while their length is 703 pixels in the case of experiment 2), are not taken into account, one finds

$$\zeta=0.83\pm0.04 \ . \tag{16}$$

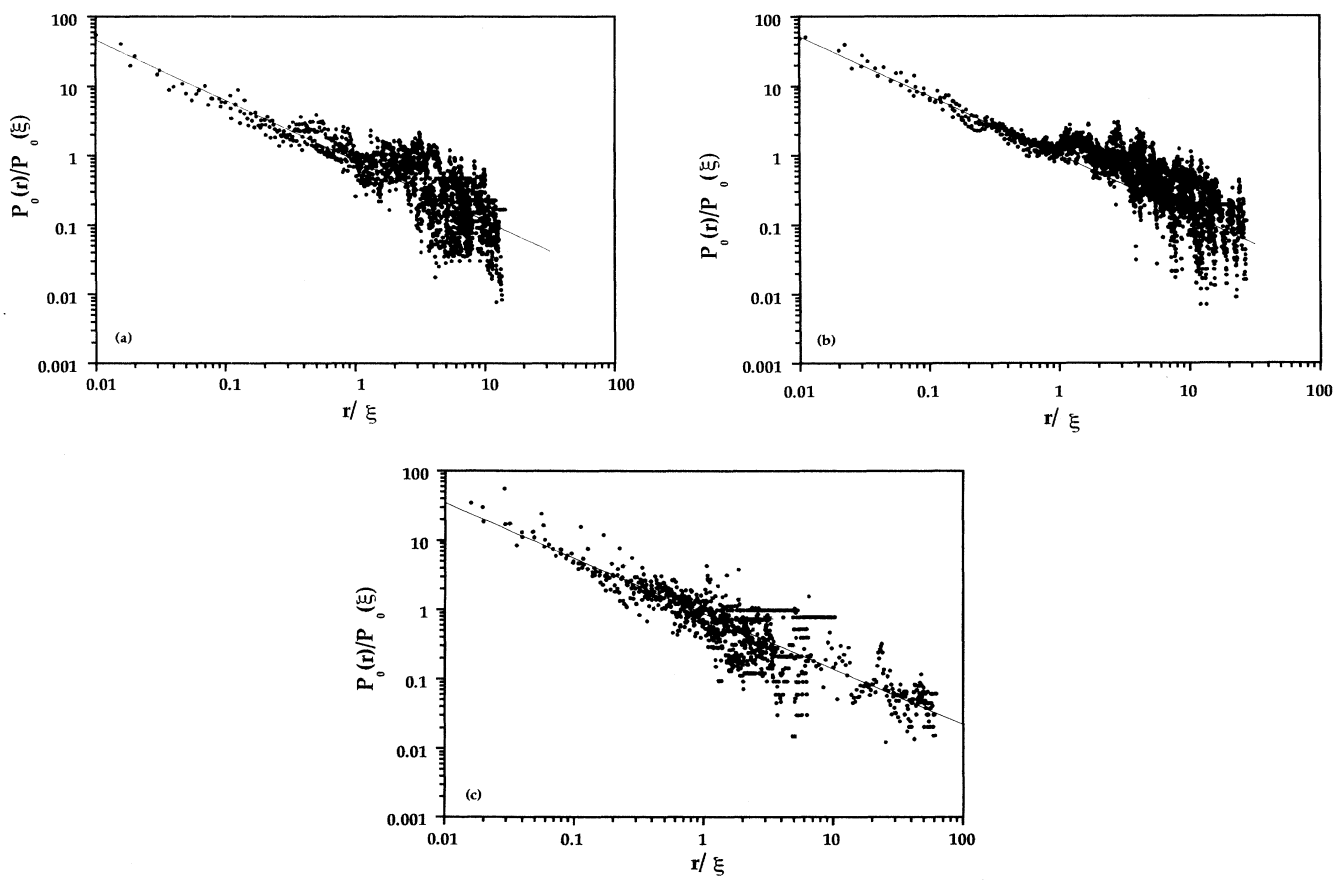

FIG. 4. Log-log plot of the return probability $P_0(r)/P_0(\xi)$ as a function of r/ξ. Curves (a), (b), and (c) correspond, respectively, to experiments 1, 2, and 3. Linear regimes extend approximately over two decades in r/ξ. The measured roughness indices ζ for each experiment, as well as the estimated correlation lengths ξ for each image are given in Table I. Let us emphasize that the scaling regime extends only up to ξ, which lies within the range of grain widths. (a) $\zeta=0.84\pm0.04$, (b) $\zeta=0.83\pm0.04$, (c) $\zeta=0.79\pm0.07$.

In any case, ζ remains close to 0.8, again excluding the minimum surface exponent, and in perfect agreement with other results on brittle[8] or ductile[1–7] materials. However, in order to quantify the "branched character" of the structure, the fluctuations of the total number of cracks must also be computed.

B. Fluctuations of the number of branches

On each image, $N(r)$ [defined by Eq. (14)] is determined, and shown to exhibit a power-law behavior for distances r smaller than the correlation length ξ. Figure 5 shows $N^2(r)/N^2(\xi)$ as a function of r/ξ in a log-log plot for the three experiments under consideration. One has

$$N(r) \sim r^b , \tag{17}$$

with

$$b = 0.13 \pm 0.03 . \tag{18}$$

However, as this exponent is relatively small, one cannot exclude that $N(r)$ might behave as $\ln(r)$. However, it has been shown recently that the exponent b could be related to dynamical parameters of crack branching during crack propagation,[38] and this will be emphasized in the next section.

C. Height probability distributions

In the case of a multivalued set of heights, at least three probability distributions can be defined. As already defined above, P and P_m describe the whole branched structure and the averaged heights. One could also define the probability distribution of the backbone. The latter will be the object of a further work. In this section, results are presented on both P and P_m. Both exhibit a long-tail behavior, although with different exponents. The complete distribution P however, is broader than P_m.

The conditional probability distribution $P(r,z)$ is the probability that (r,z) is a point of the structure knowing that the origin $(0,0)$ itself belongs to it, and thus requires further average over the origin. Only positive distances r in the horizontal plane are considered, while both positive and negative values of the difference z in heights are

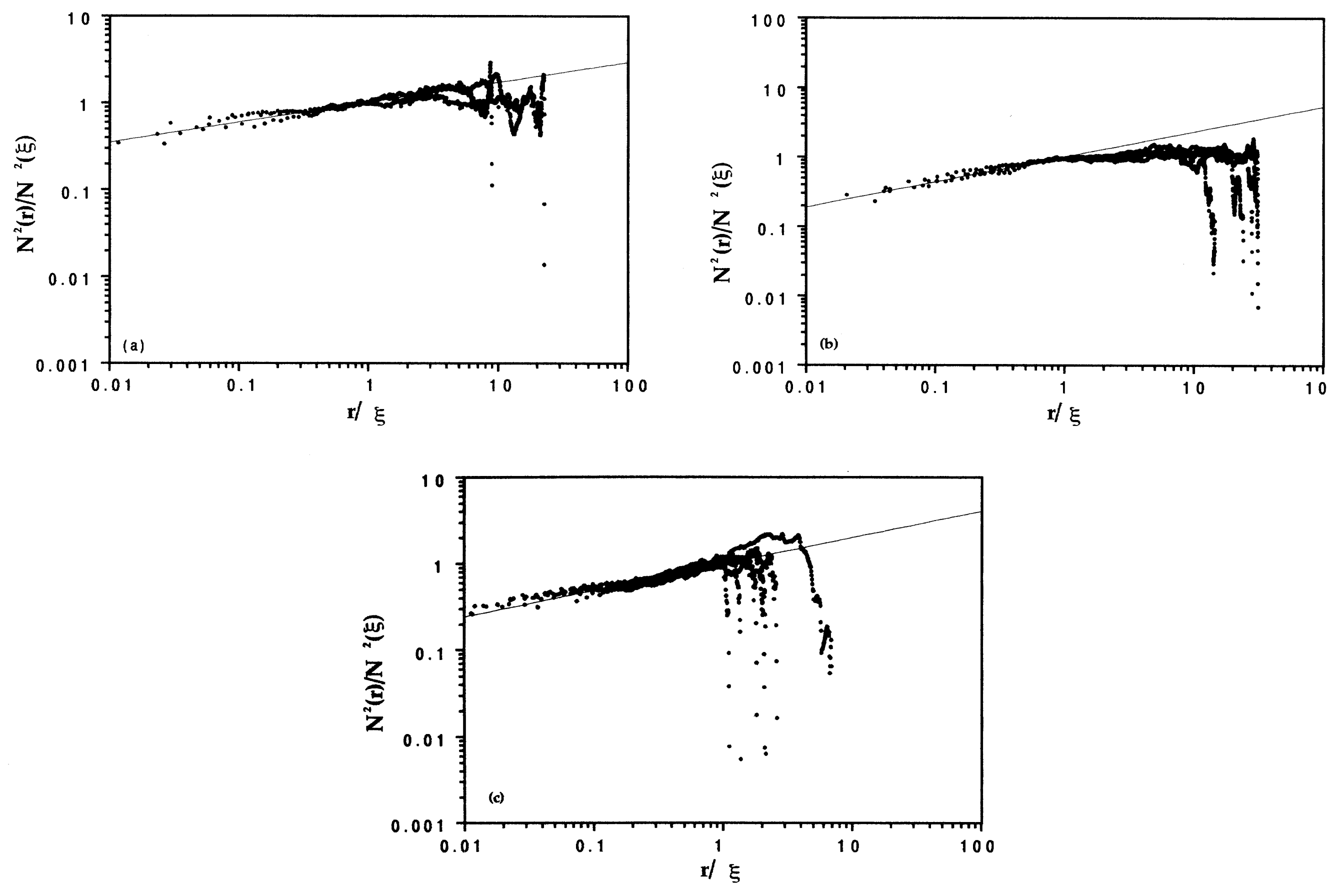

FIG. 5. Log-log plot of the fluctuations of the number of branches $N^2(r)/N^2(\xi)$ as a function of r/ξ. Curves (a), (b), and (c) correspond, respectively, to experiments 1, 2, and 3. Here again, the linear regimes extend approximately over two decades in r/ξ, and the following values of the exponent b are determined (b is half the slope determined on each set of curves): (a) $b = 0.12 \pm 0.03$, (b) $b = 0.11 \pm 0.03$, (c) $b = 0.16 \pm 0.03$. Once again, let us note that the scaling regime does not extend beyond the typical grain size.

taken into account. However, in order to improve the statistics, one makes the assumption that P is an even function of z, for fixed r,

$$P(r,z)=P(r,-z)\ . \tag{19}$$

"Boxes" of length 30 pixels are used to compute the histogram, so that 24 different values are actually taken into account. Values of r not greater than 100 pixels were taken into account for each image, because only values smaller than the correlation length ξ lie within the scaling domain. On the other hand, only the asymptotic behavior of the function f defined by Eq. (1) is of interest here, and this corresponds to high enough values of the ratio z/r^{ζ}.

The various curves $r^{\zeta}P(r,z)$ as a function of z/r^{ζ} obtained for $r=1$ to 100 pixels are shown to superimpose reasonably well for each image (see Fig. 6 for example), thus confirming the scaling hypothesis expressed in Eq. (1). Note that the width of the scaling region decreases with increasing r. It will be shown in the following that the upper cutoff z_{max} of z is approximately a constant z_0 (see Sec. III D). Thus z_{max}/r^{ζ}, which is the upper limit of the scaling domain for a given r, decreases when r increases.

In order to analyze the asymptotic behavior of f [Eq. (1)], $r^{\zeta}P(r,z)=f(z/r^{\zeta})$ is further averaged over all possible values of r for a given z/r^{ζ}. It is shown that for each image, $f(x)$ behaves like a power law $x^{-(1+\mu)}$, with an exponent μ close to 0. Error bars are difficult to estimate in this case, because of the averaging over various values of r. However, the study of a few different averages has shown that the exponent $-(1+\mu)$ always remains close to -1 (see Table I). Although the correlation length ξ for each image is not measured precisely enough to allow for a real collapse of all the spectra on the same curve, an attempt was made in Fig. 7, where the distances r and z are expressed in pixels. One can see that the five curves are reasonably linear, and nearly parallel. The measured exponent is very close to -1; however, one cannot exclude that logarithmic corrections give rise to an apparent exponent slightly smaller than -1 (~ -1.1). These corrections cannot be determined because of the statistical noise—mainly due to the relatively small size of the images.

The probability distribution P_m of the averaged height $\bar{z}(r)$ defined by Eq. (2) is also computed using boxes of length 30 pixels. P_m also scales like

$$P_m(r,\bar{z}(r))=\frac{1}{r^{\zeta}}g\left[\frac{\bar{z}}{r^{\zeta}}\right],$$

as shown on Fig. 8(a). As in the case of P, an average is performed on the values of r ranging from 1 to 100 pixels. Figure 8(b) shows that for the five images analyzed in ex-

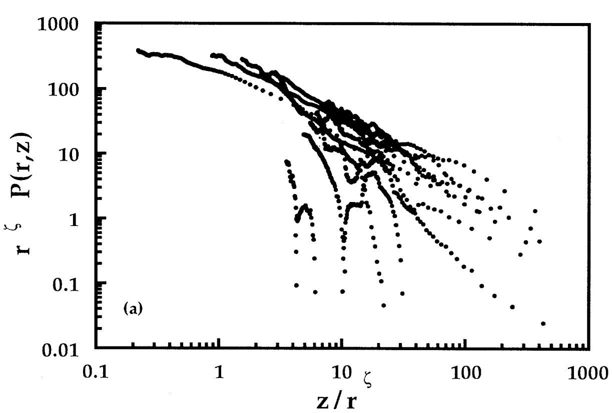

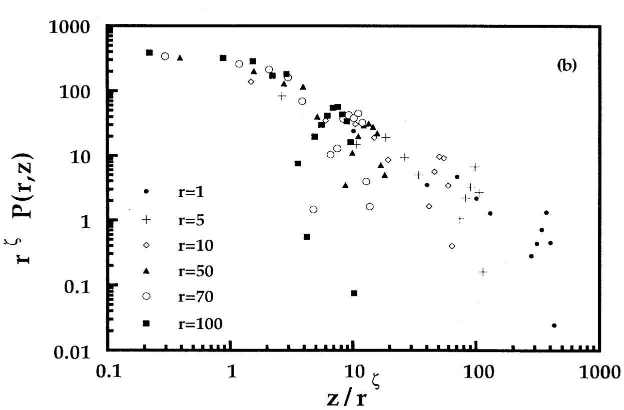

FIG. 6. Experiment 2. Image number 2/1 (see Table I). (a) $r^{\zeta}P(r,z)$ as a function of z/r^{ζ} on a log-log plot, for values of r ranging from 1 to 100 pixels. The 100 curves superimpose reasonably well up to a cutoff of the order of z_0/r^{ζ}, which decreases with increasing r. (b) Same plot as in Fig. 6(a), but only six values of r ($r=1,5,10,50,70,100$ pixels) have been superimposed.

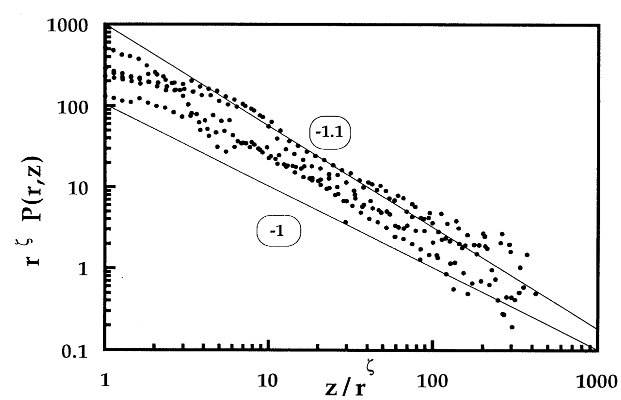

FIG. 7. Experiment 2. Distances r and z are expressed here in pixels. $r^{\zeta}P(r,z)$ was averaged over all the values of r which lead to close values of z/r^{ζ}. Linear regimes on the log-lot plot extend approximately over two decades for each micrograph. Values of the various slopes lie in Table I. On average, the exponent is close to -1.11. A line of slope -1 is also drawn to show that the actual exponent is slightly smaller than -1, but this might be due to logarithmic terms for which we could not have any evidence.

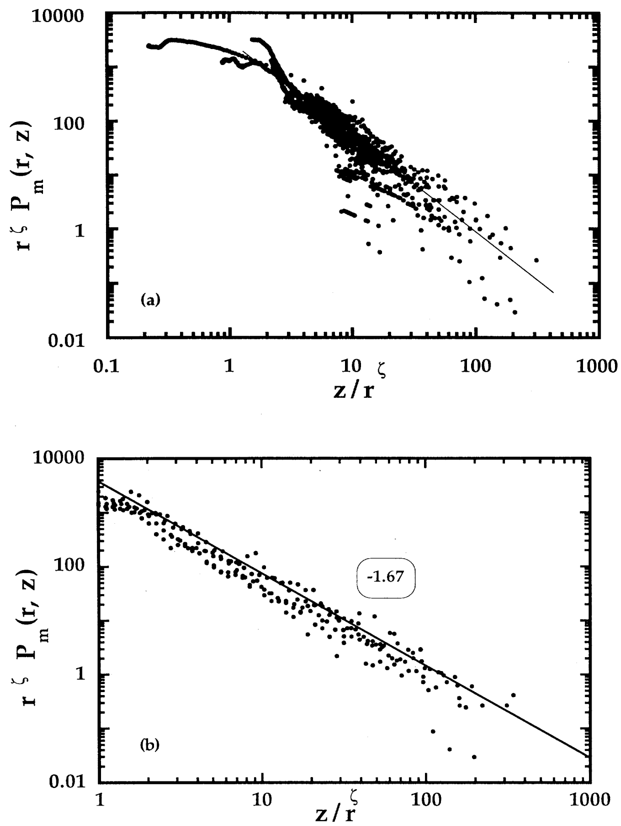

FIG. 8. Experiment 2. Image number 2/5 (see Table I). (a) $r^{\zeta}P_m(r,\bar{z})$ as a function of $\bar{z}/r^{\zeta}$ on a log-log plot, for values of r ranging from 1 to 100 pixels. As in Fig. 6, the 100 curves superimpose reasonably well, except for values of $\bar{z}/r^{\zeta}$ which give rise to particularly low values of $P_m(r,\bar{z})$. (b) Averaged value of $r^{\zeta}P_m(r,\bar{z})$ over various values of r which lead to close values of $\bar{z}/r^{\zeta}$, as a function of $\bar{z}/r^{\zeta}$, on a log-log plot. It is worth noting that the curves superimpose well with distances r and z expressed in pixels. The linear regime extending over two decades has a slope equal to -1.67 ± 0.07.

periment 2, the function g exhibits a power-law behavior

$$g(x)=\frac{1}{x^{(1+\mu')}} \tag{20}$$

with exponent (see Table I)

$$\mu'=0.67\pm0.07\ . \tag{21}$$

As it will be shown now, this value is in good agreement with the results obtained on the moments $\langle|\bar{z}(x+r)-\bar{z}(x)|^q\rangle$ of the averaged height $\bar{z}(r)$.

D. Moments of the distributions of heights

1. Infinite order moment of the distribution of heights $P(r,z)$

The moment of infinite order $z_{\max}(r)$ was determined for the distribution of heights $P(r,z)$:

$$z_{\max}(r)=\langle\{\mathrm{Max}[z(x+r')]-\mathrm{Min}[z(x+r')]\}_{0<r'<r}\rangle_x\ , \tag{22}$$

where $\{\mathrm{Max}[z(x+r')]-\mathrm{Min}[z(x+r')]\}_{0<r'<r}$ is the difference between the maximum and the minimum heights detected in a window of width r originating at point x. An average over all the possible values of x ($1<r<N-x$, where $N=703$ in experiment 2 and $N=186$ in experiment 3 is the total width of the images) is then achieved. Figure 9 shows that $z_{\max}(r)$ behaves in the following way:

$$z_{\max}(r)\simeq z_0+z_1\left[\frac{r}{\xi}\right]^{\zeta}, \tag{23}$$

where z_0 is approximately the local thickness occupied by the branches, and as a result, it varies slightly from image to image (see Table I). Note that the power-law behavior

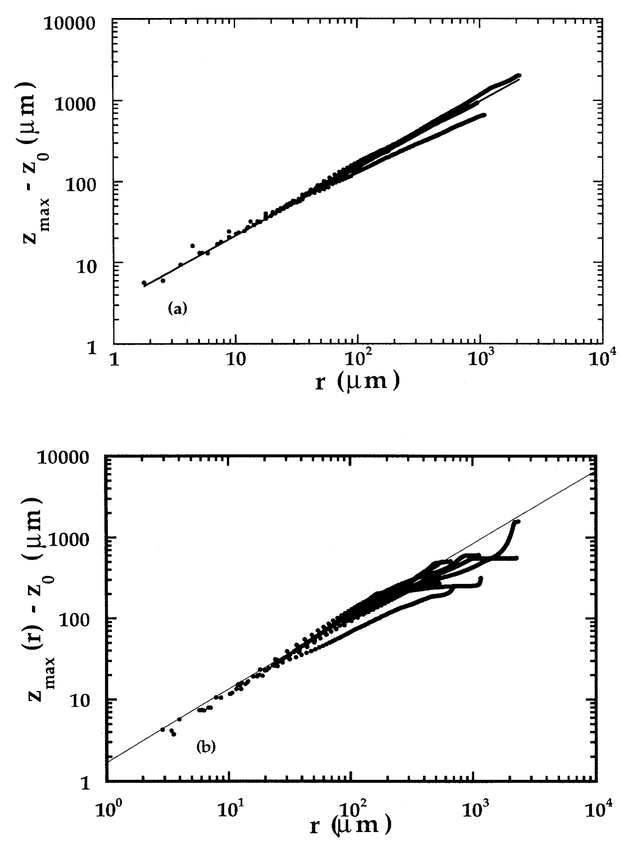

FIG. 9. Infinite order moment $z_{\max}(r)-z_0$ as a function of r, on a log-log plot. Length z_0 is on the order of the whole width occupied by the branches, and, as a consequence, its value varies slightly from image to image, as shown in Table I. (a) Experiment 2. The linear regime extends over three decades in real scale. The slope is 0.83, i.e., equal to ζ with a very good accuracy. (b) Experiment 3. The linear regime extends over two decades. The measured slope is 0.89, compatible with the value of the roughness index, although a bit higher. This slight discrepancy could originate from finite-size effects.

of $z_{\max}(r)-z_0$ *extends over three decades* in the case of experiment 2.

2. *Finite order moments of the distribution P_m of averaged heights*

Moments M_q [Eq. (5)] were determined in experiments 2 and 3 for finite values of q ($q=2,3,4,5,6$) for the distribution of averaged heights described above by the probability $P_m(r,\bar{z}(r))$. Figure 10(a) shows that the second order ($q=2$) moment of P_m behaves like a power law with exponent

$$\zeta(2)=0.71\pm0.02 \ . \tag{24}$$

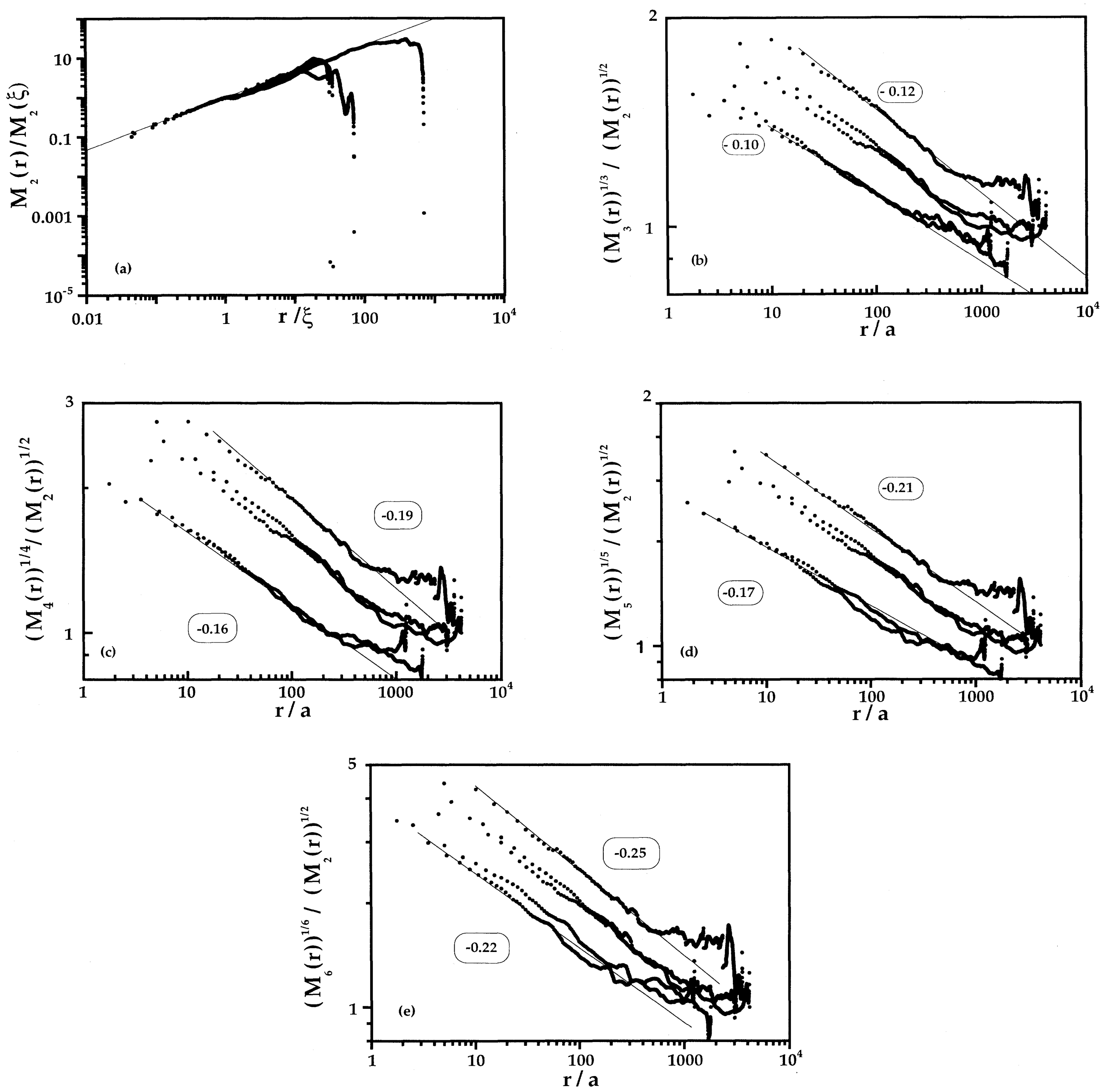

FIG. 10. Experiment 2. Moments of the distribution $P_m(r,\bar{z}(r))$ of averaged heights. (a) Log-log plot of $M_2^2(r)/M_2^2(\xi)$ as a function of r/ξ. The linear regime extending over approximately three decades allows for the determination of exponent $\zeta(2)=0.71\pm0.02$. (b) to (e) Log-log plot of ratios $[M_q(r)]^{1/q}/[M_2(r)]^{1/2}$ as functions of r/a ($a=1$ μm). The five curves present in each case linear regimes extending over more than two decades, and are reasonably parallel, thus allowing for the determination of the difference of exponents $\zeta(q)/q-\zeta(2)/2$. (b) $q=3$, $\zeta(3)/3-\zeta(2)/2=0.11\pm0.01$, (c) $q=4$, $\zeta(4)/4-\zeta(2)/2=0.18\pm0.02$, (d) $q=5$, $\zeta(5)/5-\zeta(2)/2=0.19\pm0.02$, (e) $q=6$, $\zeta(6)/6-\zeta(2)/2=0.24\pm0.02$.

Ratios of the type

$$\frac{[M_q(r)]^{1/q}}{[M_2(r)]^{1/2}} \tag{6'}$$

with $q=3,4,5,6$, are plotted versus r in Figs. 10(b)–10(e). These ratios exhibit power-law behaviors with exponents

$$\frac{\zeta(3)}{3}-\frac{\zeta(2)}{2}=-0.11\pm0.01\ , \tag{25}$$

$$\frac{\zeta(4)}{4}-\frac{\zeta(2)}{2}=-0.18\pm0.02\ , \tag{26}$$

$$\frac{\zeta(5)}{5}-\frac{\zeta(2)}{2}=-0.19\pm0.02\ , \tag{27}$$

$$\frac{\zeta(6)}{6}-\frac{\zeta(2)}{2}=-0.24\pm0.02\ . \tag{28}$$

Although these exponents are rather small, these ratios do depend on r. As will be shown below, these values are perfectly compatible with the description used in Eqs. (20) and (21).

III. DISCUSSION

The experiments described in this paper confirm the universality of the roughness exponent ζ of fracture surfaces. Let us recall in particular that it was found equal to 0.80 ± 0.05 on a series of 7475 aluminum alloys[6,7] (ductile fracture), and equal to 0.83 ± 0.05 on Ni_3Al (brittle). These values, as well as those determined in other experiments[1–9] in a comparable lengthscale regime, except the one reported in Ref. 27, rule out the value 0.5 and the hypothesis that a fracture surface could be a "standard" *minimum surface.*[23] This discrepancy does not seem to exist on bidimensional systems, where the exponent $\frac{2}{3}$ of the direct polymer in a random medium was recovered in experiments.[34,35] However, although the roughness exponent of Ni_3Al fracture surfaces, defined through the power-law behavior of the return probability P_0 is close to 0.8, their structure is much more complex than those of aluminum alloys, exhibiting deep branched cracks and overhangs. The aim of this work was to describe the whole statistics of these surfaces in order to quantify their branched character. In particular, the typical number of branches $N(r)$ is shown to exhibit a power-law behavior, involving an exponent, $b=0.13\pm0.03$. This result can be interpreted within the framework of a simple bidimensional model which will be published elsewhere,[38] but will be briefly mentioned here. One first argues that the probability of branching between r and $r+dr$ along the main crack path is uniform, and can be written

$$\frac{dr}{l_1}\ , \tag{29}$$

where l_1 is homogeneous to a length, as in a model recently proposed by Perlsman and Schwartz.[39] Then, one may show that the probability that the branches born at a distance r' from the origin are still alive at a distance r has to be of the form

$$\frac{l_2}{|r-r'|}\ . \tag{30}$$

This is a direct consequence of the scaling property of $P(r,z)$. It was also established numerically in the case of the treelike structure of directed polymers considered by Perlsman and Schwartz,[39] and analytically in the mean-field theory of branching structures.[40] l_2 is related to the average width of the structure at a given distance, which diverges logarithmically

$$\int_a^r dr'\frac{l_2}{r'}\sim l_2\ln\left[\frac{r}{a}\right]\ . \tag{31}$$

Thus the number of branches at a distance r is given by the relation

$$N(r)=\int_0^r dr'\frac{1}{l_1}\frac{l_2}{(r-r')}N(r-r')\ . \tag{32}$$

Equation (32) has a solution of the type

$$N(r)=r^b \tag{33}$$

with

$$b=\frac{l_2}{l_1}\ . \tag{34}$$

This result is however not in agreement with the one obtained by Perlsman and Schwartz,[39] who predict a logarithmic behavior of $N(r)$. Note that our experiments could as well be fitted by a logarithm, but the slope of the line depends on the micrograph.

The b exponent is thus a very interesting piece of information on the dynamics of branching during crack propagation. In our case, $b=l_2/l_1$ is approximately equal to 0.13, which means that the average time to be expected between two branching points on the backbone is approximately eight times longer than the lifetime of a branch.

In a further work,[38] we will show that the same hypothesis implies that the probability distribution of the heights $P(r,z)$ scales as

$$P(r,z)=\frac{1}{z}\quad (z\gg r^{\zeta})\ .$$

As shown earlier, this is in perfect agreement with our experimental results, for which, however, logarithmic corrections cannot be excluded. Note that the probability $P(r,z)$ no more depends on z for z high enough (in practice, for $z\geq r^{\zeta}$, see Fig. 7). It has been verified that the backbones of our structures also have roughness indexes close to 0.8. One can then think of the branched structure as a "fluffy" fractal (see Fig. 11), with branches growing on a "basement" of roughness 0.8. The validity of this image is confirmed by the behavior of $z_{\max}(r)$: $z_{\max}(r)$:

$$z_{\max}(r)\simeq z_0+z_1\left[\frac{r}{\xi}\right]^{\zeta}\ ,$$

[Eq. (23)], the upper frontier of the branched structure of width z_0 having the same roughness 0.8 as the backbone.

As discussed above, the probability of the distribution of averaged heights $P_m(r,\bar{z}(r))$ is also found to be broad:

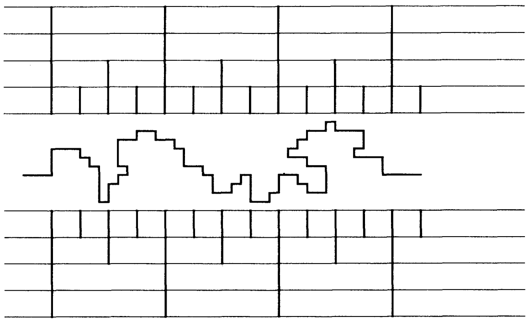

FIG. 11. Sketch of the "fluffy" fractal. Branches grow on a backbone which still contains some "connected" overhangs (thus z is not everywhere single valued on the backbone). However, the roughness index of this backbone is also 0.8. When far enough from the backbone, the probability distribution of heights $P(r,z)$ is independent of r, and scales as $1/z$. This decaying density of points belonging to branches around the backbone is pictorially represented by thick segments.

$$P_m(r,\bar{z}(r)) = \frac{1}{r^{\zeta}} \left[\frac{\bar{z}}{r^{\zeta}} \right]^{-1-\mu'} .$$

The value $\mu' = 0.67$ is in agreement with the results found on the moments

$$\langle z^q \rangle = \int_a^{z_{\max}} \frac{dz}{r^{\zeta}} z^q \left[\frac{z}{r^{\zeta}} \right]^{-1-\mu'}$$
$$= r^{\mu'\zeta}(z_{\max}(r))^{(q-\mu')} . \quad (35)$$

As the leading term in $z_{\max}$ is constant, apparent exponents $\zeta(q)$ are equal to

$$\zeta(q) \simeq \mu'\zeta + \zeta_{\max}(q-\mu') , \quad (36)$$

where $\zeta_{\max} \simeq 0.1$ is an "effective" exponent characterizing $z_{\max}$:

$$z_{\max}(r) \simeq z_0 + r_1 \left[\frac{r}{\xi} \right]^{\zeta} \sim r^{0.1} . \quad (37)$$

This is in rather good agreement with the results expressed in Eqs. (24)–(28).

A further work should compare the properties of the backbone to those of the whole structure. The analysis of a profile parallel to the direction of the crack propagation should also reveal particularly useful. Furthermore, a comparison between the statistics of the branched and nonbranched fracture surfaces of the same material should be particularly rich. This could be performed on an aluminum alloy of the 7000 series subjected to fatigue.[17] For low enough fixed ΔK values, the crack velocity is low enough, and the fracture surface exhibits no branches. If ΔK overpasses a critical value, branching occurs, while the measured velocity of the main crack sticks to its critical value.

A careful study of the modifications of the fracture surface statistics at the onset of the "branching transition" should also give information on the nature of the micromechanisms responsible for crack propagation and branching. This information could be particularly relevant in the case of intermetallics, subjected to drastic changes in fracture mode due to dynamical effects.

ACKNOWLEDGMENTS

We are particularly grateful to Professor G. I. Barenblatt for the interest he took in our work, and for making a very important remark. We are also indebted to J.-P. Bouchaud for enlightening discussions, constant support, and a critical reading of the manuscript. We want to express our gratitude to S. Roux and A. Hansen, with whom the discussions were particularly fruitful. Metallographic help from L. Rolly is gratefully acknowledged, as well as useful advice from D. Boivin and J.-L. Pouchou. We also thank J.-L. Raffestin for elaborating the material and P. Josso for accepting to plate one of our samples. Finally, part of this work has been achieved while one of us (E.B.) was on leave at the University of Cambridge, under a contract of the French Ministry of defense, DRET No. 92/1437/A000. She wishes to express her gratitude to the DRET and to the University of Cambridge, and particularly to J. King for hospitality. Computing advice from A. Boyd-Lee, and discussions with A. Gingell and D. Baxter as well as A. Gingell's help on the manuscript were also highly appreciated.

[1]B. B. Mandelbrot, D. E. Passoja, and A. J. Paullay, Nature (London) **308**, 721 (1984).
[2]J. J. Mecholsky, D. E. Passoja, and K. S. Feinberg-Ringel, J. Am. Ceram. Soc. **72**, 60 (1989).
[3]R. H. Dauskardt, F. Haubensak, and R. O. Ritchie, Acta Metall. Mater. **38**, 143 (1990).
[4]Z. Q. Mu and C. W. Lung, J. Phys. D **21**, 848 (1988).
[5]M. Tanaka, J. Mater. Sci. **27**, 4717 (1992).
[6]E. Bouchaud, G. Lapasset, and J. Planès, Europhys. Lett. **13**, 73 (1990).
[7]E. Bouchaud, L. de Arcangelis, G. Lapasset, and J. Planès, La Recherche (Paris) **22**, 808 (1991).
[8]K. J. Måløy, A. Hansen, E. L. Hinrichsen, and S. Roux, Phys. Rev. Lett. **68**, 213 (1992).
[9]A. Imre, T. Pajkossy, and L. Nyikos, Acta Metall. Mater. **40**, 1819 (1992).
[10]B. B. Mandelbrot, Phys. Scr. **32**, 257 (1985).
[11]A. Hansen, E. L. Hinrichsen, and S. Roux, Phys. Rev. Lett. **66**, 2476 (1991).
[12]K. Aoki, Trans. Jpn. Inst. Met. **31**, 443 (1990).
[13]Observations have been made on the Super-α_2 Ti_3Al-based alloy by A. Lemoine, E. Bouchaud, G. Lapasset, and M. Thomas, and on TiAl by I. Phan, G. Hug, and G. Lapasset (unpublished).
[14]B. R. Lawn and T. R. Wilshaw, *Fracture of Brittle Solids* (Cambridge University Press, Cambridge, 1975), Chap. 5, p. 10.
[15]J. E. Field, Contemp. Phys. **12**, 1 (1971).

[16]E. H. Yoffe, Philos. Mag. **42**, 673 (1951).
[17]A. Gingell, D. Baxter, and J. King (unpublished).
[18]K. Ravi-Chandar and W. G. Knauss, Int. J. Fract. **26**, 65 (1984).
[19]K. Ravi-Chandar and W. G. Knauss, Int. J. Fract. **26**, 141 (1984).
[20]J. Fineberg, S. P. Gross, M. Marder, and H. L. Swinney, Phys. Rev. Lett. **67**, 457 (1991).
[21]J. S. Langer, Phys. Rev. A **46**, 3123 (1992).
[22]A. Hansen, C. Poirier, J.-P. Troadec, K. J. Måløy, S. Roux, and E. L. Hinrichsen (unpublished).
[23]S. Roux and D. François, Scr. Metall. **25**, 1092 (1991).
[24]M. Kardar and Y.-C. Zhang, Europhys. Lett. **8**, 233 (1989).
[25]M. Mézard and G. Parisi, J. Phys. I (France) **1**, 809 (1991).
[26]T. Halpin-Healy, Phys. Rev. A **42**, 711 (1990).
[27]P. Mc Anulty, L. V. Meisel, and P. J. Cote, Phys. Rev. A **46**, 3523 (1992).
[28]V. Y. Milman, R. Blumenfeld, N. A. Stelmashenko, and R. C. Ball (unpublished).
[29]V. Y. Milman, N. A. Stelmashenko, R. Blumenfeld, and R. C. Ball (unpublished).
[30]L. de Arcangelis and H. J. Herrmann, Phys. Rev. B **39**, 2678 (1989).
[31]*Statistical Models for the Fracture of Disordered Media,* edited by H. J. Herrmann and S. Roux (Elsevier, Amsterdam, 1990).
[32]M. Kardar, Nucl. Phys. B **290**, 582 (1987).
[33]T. Halpin-Healy, Phys. Rev. A **44**, R3415 (1991).
[34]J. Kertész, V. K. Horvath, and F. Weber, Fractals **1**, 67 (1993).
[35]C. Poirier, M. Ammi, D. Bideau, and J.-P. Troadec, Phys. Rev. Lett. **68**, 216 (1992).
[36]C. Vanneste and D. Sornette, J. Phys. I (France) **2**, 1621 (1992).
[37]J. Feder, *Fractals* (Plenum, New York, 1988).
[38]J.-P. Bouchaud, E. Bouchaud, J. Planès, and G. Lapasset (unpublished).
[39]E. Perlsman and M. Schwartz, Europhys. Lett. **17**, 11 (1992).
[40]P. Alstrom, Phys. Rev. A **38**, 4905 (1988).

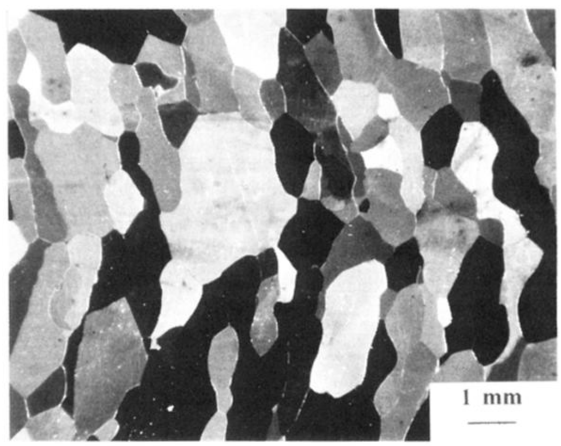

FIG. 1. Optical macrograph showing the etched surface (Fry Etch) of the Ni_3Al material prior to fracture. One can note that the metallurgical grains are not isotropic; they are in fact elongated in the direction of the main crack. Both lengths and widths of the grains in the polishing plane appear to be rather broadly distributed.

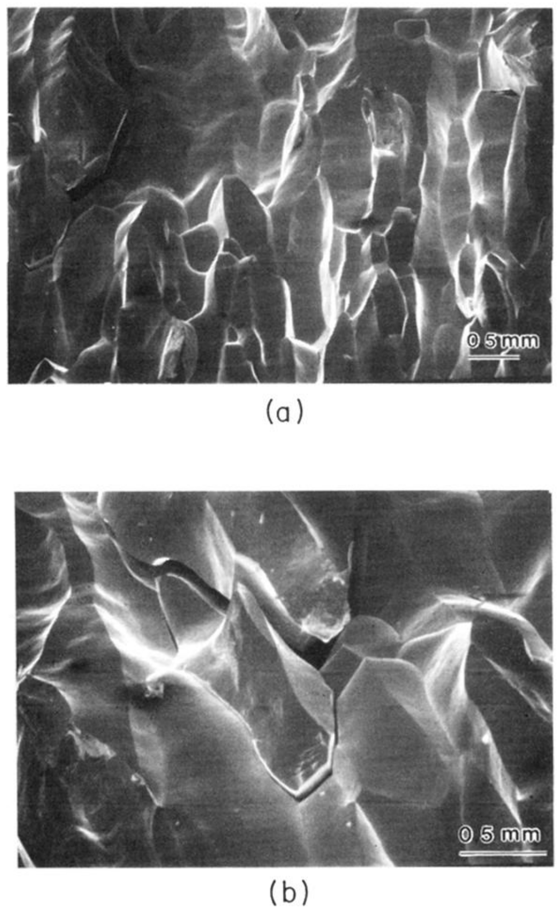

FIG. 2. Micrographs taken with a scanning electron microscope Cambridge Stereoscan 100. (a) and (b) both show the fracture surfaces, at two different magnifications. The fracture mode is clearly intergranular. (a) gives an idea of the anisotropy of the grains, as well as of the broad character of their widths distribution. (b) clearly shows the presence of deep secondary cracks.

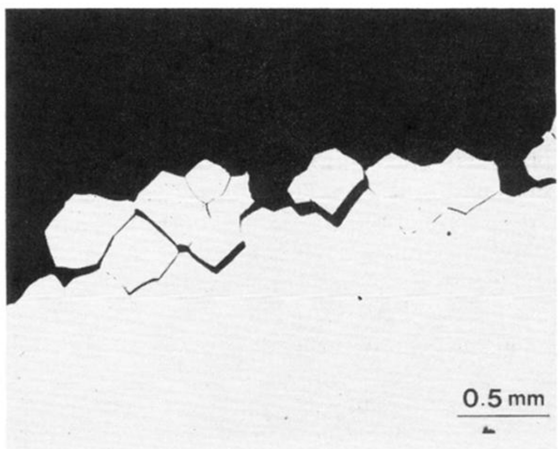

FIG. 3. Experiment 1. Optical micrograph Olympus PMG3. The fracture surface is coated with an opaque resin. The "vertical" cut reveals a branched profile. Note also the presence of overhangs, linked to the fracture surface in planes located beside the polishing plane.